

# Supplementary materials for "Sufficient sampling for kriging prediction of cortical potential in rat, nonhuman primate, and human $\mu$ ECoG"

Michael Trumpis<sup>1</sup>, Chia-Han Chiang<sup>1</sup>, Amy L. Orsborn<sup>2,3,4,5</sup>, Brinnae Bent<sup>1</sup>, Jinghua Li<sup>6,7,8</sup>, John A. Rogers<sup>6,9,10,11</sup>, Bijan Pesaran<sup>5</sup>, Gregory Cogan<sup>12,13,14,15</sup> and Jonathan Viventi<sup>1,16</sup>

<sup>1</sup>Department of Biomedical Engineering, Duke University, Durham, NC 27708, USA.

<sup>2</sup>Department of Electrical & Computer Engineering, University of Washington, Seattle, WA 98195, USA

<sup>3</sup>Department of Bioengineering, University of Washington, Seattle, WA 98105, USA

<sup>4</sup>Washington National Primate Research Center, Seattle, WA 98195, USA

<sup>5</sup>Center for Neural Science, New York University, New York, NY, USA

<sup>6</sup>Department of Materials Science and Engineering, Northwestern University, Evanston, IL 60208, USA

<sup>7</sup>Department of Materials Science and Engineering, The Ohio State University, Columbus, OH 43210, USA

<sup>8</sup>Chronic Brain Injury Program, The Ohio State University, Columbus, OH 43210, USA

<sup>9</sup>Simpson Querrey Institute, Northwestern University, Chicago, IL 60611, USA.

<sup>10</sup>Department of Biomedical Engineering, Northwestern University, Evanston, IL 60208, USA.

<sup>11</sup>Department of Neurological Surgery, Feinberg School of Medicine, Northwestern University, Chicago, IL 60611, USA.

<sup>12</sup>Department of Neurosurgery, Duke School of Medicine, Durham, NC 27710, USA.

<sup>13</sup>Department of Psychology and Neuroscience, Duke University, Durham, NC 27708, USA.

<sup>14</sup>Center for Cognitive Neuroscience, Duke University, Durham, NC 27708, USA.

<sup>15</sup>Duke Comprehensive Epilepsy Center, Duke School of Medicine, Durham, NC 27710, USA.

<sup>16</sup>Department of Neurobiology, Duke School of Medicine, Durham, NC 27710, USA.

## 1 Covariance estimation

The spatial covariance kernel model we used for all  $\mu$ ECoG fields was the positive-definite Matérn kernel

$$C_{\eta}(h) = \frac{\lambda 2^{1-\nu}}{\Gamma(\nu)} \left( \frac{\sqrt{2\nu}h}{\theta} \right)^{\nu} \mathcal{K}_{\nu} \left( \frac{\sqrt{2\nu}h}{\theta} \right) \quad (1)$$

where  $\mathcal{K}_{\nu}$  is the modified Bessel function of the second kind with order  $\nu$  [1]. The length  $\theta$  scales the correlation range, and the unit-less shape parameter  $\nu$  represents the smoothness of the field at short range. Specifically,  $\lfloor \nu \rfloor$  indicates the number of times the process is mean-square differentiable. A value of  $\nu = 0.5$  corresponds

to an exponential decay function, indicative of a locally rough field (see models in [2, 3, 4]). Higher values introduce a concavity at short range that accounts for increasing local smoothness. Properties of Matérn model variograms with different ranges and degrees of smoothness are demonstrated in supplemental figure 1(a)-(c).

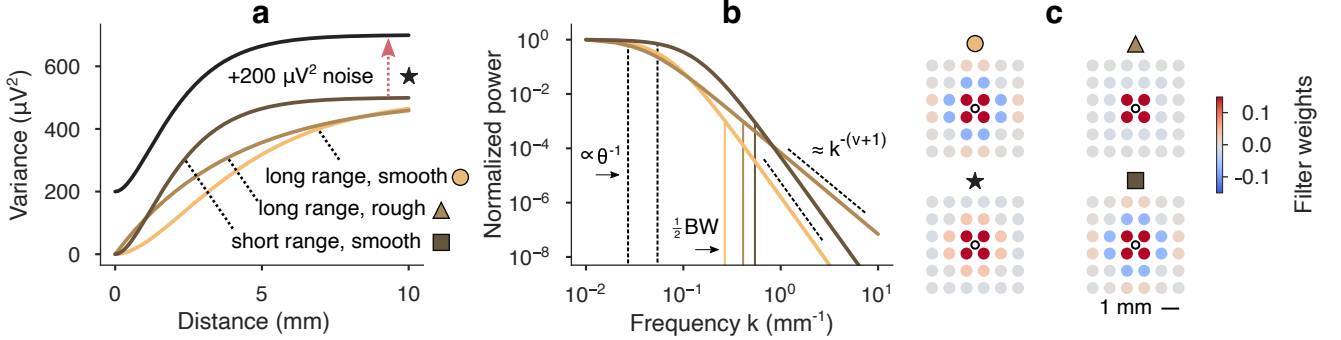


Figure S1: Kernel models and optimal prediction. (a) Example Matérn covariance kernels were parameterized by range (short range  $\theta = 2$  mm, long range  $\theta = 4$  mm), smoothness (rough  $\nu = 0.5$ , smooth  $\nu = 1.5$ ), process power ( $\lambda = 500 \mu\text{V}^2$ ), and noise power (“nugget” effect,  $\sigma_n = 200 \mu\text{V}^2$  for  $\star$ ). Total field power is the “sill”  $\zeta = \lambda + \sigma_n$ . (b) The range and texture image statistics influence the distribution of low and high spatial frequencies, respectively, in the power spectral density (PSD). Range affects the size of the main “pass band” lobe, and smooth texture creates a steeper “stop band” roll-off than rough texture. We used an effective bandwidth at -30 dB in the PSD to define the Nyquist pitch  $\Delta_{nyq} = BW^{-1}$  ( $\bullet$  1.9 mm,  $\blacktriangle$  1.3 mm,  $\blacksquare$  0.94 mm). (c) Kriging predictors for the point in the center of a 6×6 grid spaced at 1 mm were MSE optimal for each kernel. Predictors for smooth texture ( $\blacksquare$  and  $\bullet$ ) used a larger radius of samples than the predictor for rough texture ( $\blacktriangle$ ). With added noise, the optimal sharpening filter for  $\blacksquare$  was converted to a noise-reducing smoothing filter ( $\star$ ).

The spatial power spectral density (PSD) was calculated from the neural field covariance using the Fourier transform of Eq 1

$$S_n(k) \propto \left[ \frac{2\nu}{\theta^2} + (2\pi k)^2 \right]^{-(\nu+1)} \quad (2)$$

Here, the range  $\theta$  modifies the main-lobe corner frequency, and smoothness  $\nu$  affects the high frequency roll-off, similar to the time constant and order of an analog resistor-capacitor filter.

The spatial variogram analysis that we employed differed in subtle ways from other studies of correlation by distance [2, 3, 5, 6, 4]. The most salient difference is a focus on the nature of *dissimilarity* at short range. Interpreting dissimilarity is made simpler by the axiomatic meaning of  $\gamma(0) = 0$  (zero residual variance at zero distance). In contrast, the Pearson correlation coefficient estimator used in correlograms is more complicated. The per-definition  $\rho(0) = 1$  unit value of correlation requires normalization by standard deviation estimates, which lump together signal and noise, and are subject to standard error. Also, the semivariance estimator  $\gamma_x(s, u) = \frac{1}{2} \text{var}\{x_s - x_u\}$  is indifferent to electrical reference or any constant re-referencing scheme (e.g. common-averaging referencing) that greatly affects the interpretation of a correlogram curve. Focusing on short-range dissimilarity free of compounded estimator error provided a clearer view of the noise and smoothness properties that were critical factors for kriging analysis of sampling predictability.

Spatial variation was considered via spatial spectral analysis in early work with rabbit and human ECoG [7, 8], and later in rat [9]. These studies utilized strip electrodes of 64 contacts [8] or 16 contacts [9] spaced at 0.5 mm, and computed periodogram estimates of spatial PSDs. As seen in figure S2, PSDs can also be modeled with the Matérn spectral density function (eq 2). However, both covariance parameters were distorted

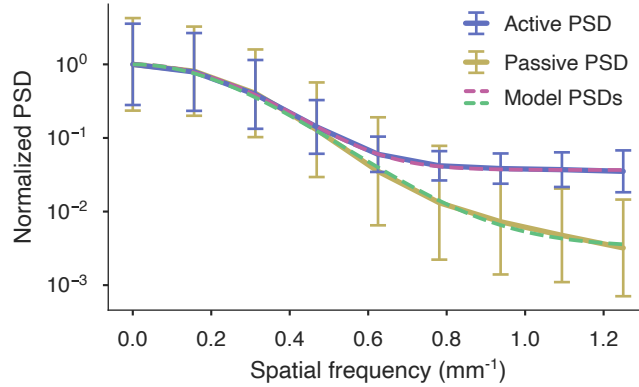


Figure S2: Computed and model  $\mu$ ECoG spatial power spectra. Spatial PSDs were computed via periodogram by applying a Hamming taper and zero-padding the rows and columns to 16 points. Vertical and horizontal PSDs were averaged for a single 500 ms block of acute  $\mu$ ECoG recording (solid lines with SD error bars). Range, smoothness, and noise floor parameters were optimized to fit Matérn spatial spectra (dashed lines) to the normalized spectra. The optimized parameters were  $\theta = 729 \mu\text{m}$  and  $\nu = 13.2$  for the active PSDs and  $\theta = 736 \mu\text{m}$  and  $\nu = 4.67$  for the passive PSDs. Note that the range parameters are underestimated due to spectral smoothing introduced by the Hamming taper: the apparent width of the main lobe is upward biased. The smoothness parameters are overestimated because the spectral roll-offs are confounded by the noise floors.

by spectral estimation. The size of the main-lobe was inflated due to spectral bias introduced by the finite sampling window, which biased the estimation of the range parameter (although this bias would reduce with a larger sampling area). The smoothness affects the roll-off behavior of the spectrum (figure S1(b)), but the noise floor confounded or even obscured this feature, complicating estimation.

## 2 Kriging analysis of auditory cortex fields with simulated noise

We tested the theoretical effects of noise on prediction error by adding controlled amounts of additive Gaussian white noise (AGWN) to  $\mu$ ECoG recorded in rat auditory cortex. For the purpose of this analysis, we treated the low-noise passive array recordings (0.48% median noise, 0.36%-0.65% IQR) as virtual noise free ground truth fields. We performed covariance modeling and kriging prediction on 3081 short-time 500 ms batches of signal in the 5-100 Hz bandpass. After fitting a covariance model and performing cross-validated prediction for each short-time field, we repeated prediction after adding AGWN to the signal in increments of 5% until 65%. Noise variance was computed in proportional to the sill variance of the individual snapshots, to normalize SNR. Prediction error was referenced to the noise-free fields, and thus free of additive noise.

The relative mean square error (relMSE) of kriging prediction inversely depended on the feature scale of  $\mu$ ECoG fields, quantified by the Nyquist pitch (figure S3(a)). The expected kriging error closely explained the cross-validated residual error (OLS slope  $b = 0.99$ ,  $r^2 = 0.912$ ). Note that the 0% noise level duplicates the result as figure 5 in the main text. Increased signal noise primarily biased prediction relMSE to higher levels, but also increased the rate at which relMSE increased at finer Nyquist pitch. Sampling predictability is depicted in figure S3(b) as a sequence of sets of Matérn models. For example, the first set are fields predictable only at 0% noise, while the next set are predictable up to 5% noise (but excluding the preceding set). The successive sets show a shift of the 10% relMSE predictability boundary to lower resolution fields, as in figure 3 in the main text. As a consequence, the kriging resolution electrode spacing that is sufficient to stabilize prediction error at 10% relMSE shifts to smaller values in an approximately log-linear fashion with increased noise levels (figure S3(c)). We quantified the median kriging error relative to each noise level in figure S3(d), which confirmed that,

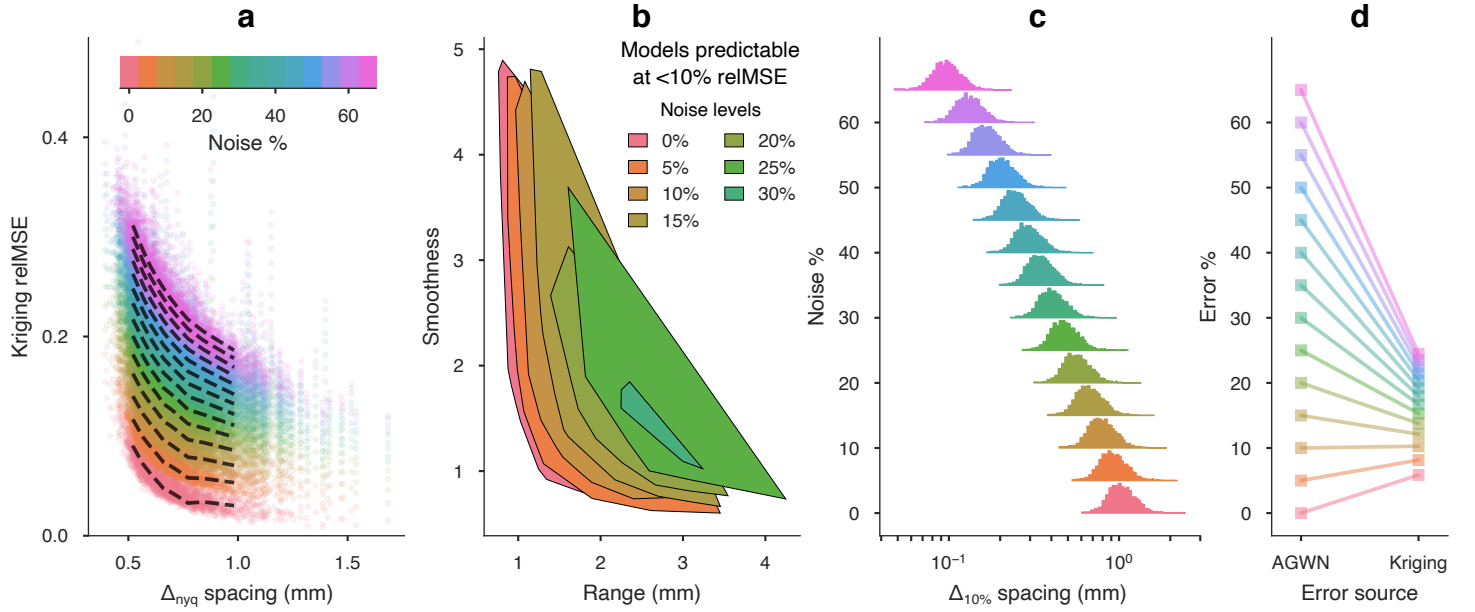


Figure S3: Predictability of artificially noised  $\mu$ ECoG fields. Additive Gaussian white noise (AGWN) from 5% to 65% was introduced to acute recordings (with approximately 0% noise) before interpolating frames by kriging. (a) AGWN worsened interpolation error, with slightly stronger interactions between high bandwidth-small scale fields and larger noise levels. The dashed lines trace the mean theoretical relMSE at each decile of the Nyquist pitch. Linear regression showed strong correspondence between theoretical and observed relMSE ( $\beta = 0.99$ ,  $r^2 = 0.91$ ). (b) Convex hull outlines of the sets of Matérn models that were 10% relMSE predictable at  $N\%$  noise. Beyond 30% noise, no fields were 10% relMSE predictable. (c) Distributions for kriging resolution shifted to smaller electrode spacings in an approximately log-linear fashion with increasing noise. (d) Median values of the two components of total cross-validated error: measurement distortion (AGWN) and kriging error.

at higher noise levels, interpolated fields are a more faithful estimate of the true neural field than even the raw measurements, in a MSE sense. For comparison,  $\mu$ ECoG recorded with the active array had a median noise level of 18.5% and a noise-compensated kriging relMSE of 9.3%.

We directly investigated the denoising property of kriging by simulating AGWN in virtually noise-free  $\mu$ ECoG fields, as described above. To study filtering efficiency, we computed kriging filters and predicted field values at the sampled electrode sites, rather than interpolating to new sites. Superficially, the kriging error equation for filtering shows that the error must be less than the noise. However, the validity of the kriging error is conditional on the covariance model. Using virtually noise-free  $\mu$ ECoG fields, we found that the model-based kriging error was a highly accurate estimate of the true filtering relMSE (OLS slope  $b = 1.04$ ,  $r^2 = 0.946$ ). The effects of feature scale (Nyquist pitch) and noise on filtering error (figure S4(a)) were analogous to the effects on interpolation error. Increased amounts of noise moved the boundary of covariance models that could be filtered to 10% relMSE in similar fashion as noise shifting the interpolation predictability boundary (figure S3(b)). Median filtering error increased with AWGN levels, while the denoising ratio also increased with noise (figure S3(c)). Although the apparently guaranteed denoising gain is conditional on the fitness of the covariance model, we found that the actual filtering error was less than every AWGN level in each of the 3081 snapshots.

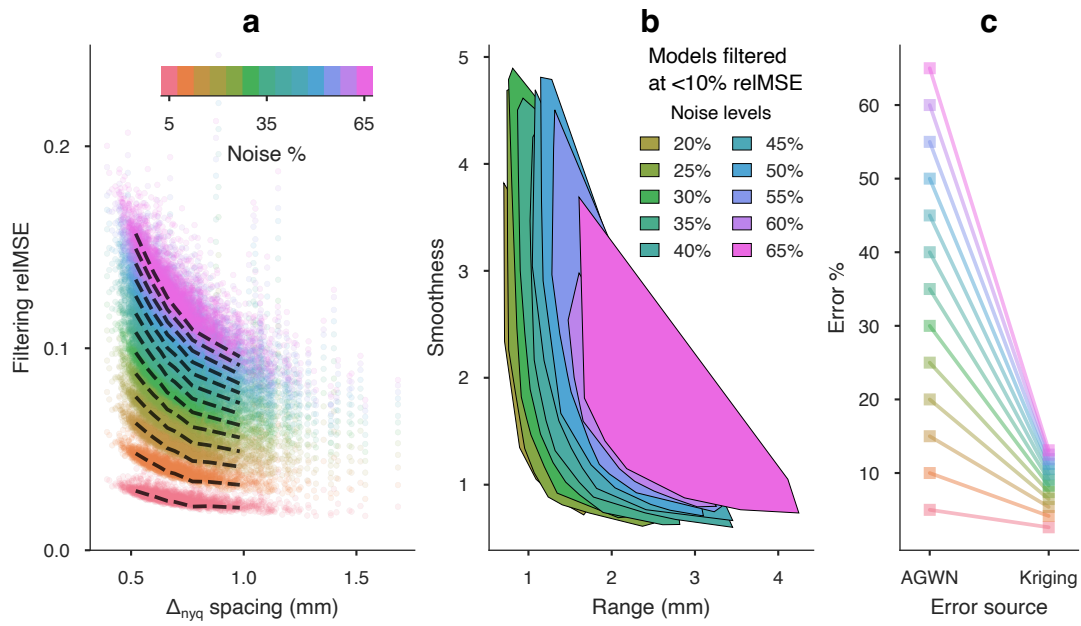


Figure S4: Denoising efficiency in artificially noised  $\mu$ ECoG fields. Additive Gaussian white noise (AGWN) from 5% to 65% was introduced to acute recordings (with approximately 0% noise) before filtering frames by kriging. (a) Filtering error deteriorated in higher AGWN, as expected by the model based kriging error. The dashed lines trace the mean theoretical reIMSE at each decile of the Nyquist pitch. Linear regression showed strong correspondence between theoretical and observed reIMSE ( $\beta = 1.04$ ,  $r^2 = 0.946$ ). (b) Convex hull outlines of the sets of Matérn models that were filtered at 10% reIMSE in N% noise. (d) Filter error (right) increased with higher AGWN (left), but the noise reduction ratio also increased.

### 3 Strengths and limitations of covariance analysis and kriging

The sum of theoretical kriging error and estimated noise generally predicted frame interpolation error accurately, with most OLS regression slopes ranging between  $\pm 10\%$  of a one-to-one relationship. Results on the mathematical and statistical stability of the kriging predictor compared to kriging mean square error (MSE) are summarized in detail in [10, 11]. The kriging predictor itself is fairly robust (in both the linear operator and the statistical predictor senses) to misspecification of the variogram model. On the other hand, the expected MSE  $\sigma_e = \lambda - c(s')^T C_x^{-1} c(s')$  tends to overestimate the realized error for highly correlated samples and in higher SNR, which agrees with the smaller regression slopes from theta bands in human and NHP. When samples are less correlated or noisier, the expected MSE tends to underestimate realized error, which may also be seen in the larger slopes in gamma and higher bandpasses.

Unlike other local interpolators such as splines, the kriging interpolator adapts naturally to SNR. The “nugget” value pads the diagonal of the data autocovariance matrix such that the BLUP solution  $w_{s'} = [C_\eta + \sigma_n I]^{-1} c(s')$  is formally equivalent to a Tikhonov (or  $\ell_2$ -norm) regularized solution. As such, the predictor weights adapt by reducing the quadrature sum of iid noise. Figure S1(c) demonstrates how a kriging filter changes from a sharpening filter to a smoothing filter to minimize prediction error in a higher noise field. When filtering sampled data *in situ* as in figure S3 (rather than predicting unsampled signals), the simple kriging BLUP is identical to a Wiener filter.

We employed a minimal field + noise signal model in the preceding analysis. The noise model was justified by its explanation of the semivariogram’s vertical offset in known noisy conditions in the active array recording, for example, and also due to its correlation with electrode impedance in a chronic implant study [12]. However, it is also possible that one or more physiological processes that become decorrelated within 400  $\mu\text{m}$  contributed to the minimum residual variance between sites at every inter-electrode distances. Based on the evidence linking high frequency field potential to neuronal spiking [13, 14, 15, 16, 17] and the observed spatial localization of high frequency ECoG [18, 19, 20], the contribution of a hypothetical small-scale process is most plausible in high frequency bands. We are currently designing  $\mu\text{ECoG}$  arrays with variable inter-electrode distances to investigate this possibility.

### 4 Kriging analysis videos

Each supplemental video shows kriging results from one full 500 ms frame of a micro-ECoG recording. The variogram and estimated kernel are shown in the left panel. Boxes and vertical stripes represent the median and interquartile range of semivariance values at spatial lags binned at  $\sim 400 \mu\text{m}$  intervals. Box edge size and line thickness are proportional to the number of electrode pairs within a bin. The heat-map frames show electrode voltage from the electrode array normalized to  $\pm 1$ . From left to right these frames are: the recorded electrode signal; the composite kriged field potential from 4X spatial subsampling; the “filtered” signal (field potential predicted at electrode locations); and the kriged potential on a grid with 4X higher density than the electrode array. The filtered frames are the best estimate of the noise-free cortical potential, conditioned on the accuracy of the variogram kernel. The high density image is a combination of on-electrode and between-electrode prediction. A timeseries plot shows the recorded potential from electrodes located in each array quadrant (TL: top-left, TR: top-right, etc.). The current sample mapped in the frames is marked by the vertical bar.

#### 4.1 Acute rat auditory cortex (supplemental videos S1-S4)

Kernel estimates and kriging statistics in tables 1-3.

Table S1: Variogram kernel parameters.

Video	$\Delta_{nyq}$ mm	$\theta$ mm	$\nu$	$\sigma_n$ $\mu V^2$	$\zeta$ $\mu V^2$	$\lambda$ $\mu V^2$	$\Delta_{10\%}$
vid S1 (passive)	0.70	1.33	1.99	36.75	4024.14	3987.39	1.19
vid S2 (active)	1.07	2.14	1.76	1029.00	11837.56	10808.56	1.46
vid S3 (passive)	0.48	1.19	1.02	26.25	3248.19	3221.94	0.67
vid S4 (active)	0.87	2.48	0.69	1029.00	6630.99	5601.99	0.54

Table S2: Cross-validated kriging results. Percentages relative to signal variance ( $\zeta$ ).

Video	CV err $\mu V^2$	CV err %	theor. err total %	noise %	kriging err %
vid S1 (passive)	199.93	4.97	4.66	0.91	3.74
vid S2 (active)	1497.66	12.65	12.91	8.69	4.22
vid S3 (passive)	433.33	13.34	15.52	0.81	14.71
vid S4 (active)	1759.38	26.53	28.05	15.52	12.53

Table S3: High-density kriging results. Percentages relative to process variance ( $\lambda$ ). (These are estimates only, and not measurable.)

Video	on-site err $\mu V^2$	on-site err %	off-site err $\mu V^2$	off-site err %
vid S1 (passive)	23.84	0.60	29.87	0.75
vid S2 (active)	192.49	1.78	192.68	1.78
vid S3 (passive)	24.15	0.75	128.99	4.00
vid S4 (active)	357.61	6.38	431.21	7.70

## 4.2 Human motor cortex 4-300 Hz (supplemental videos S5-S7)

Kernel estimates and kriging statistics in tables 4-6.

Table S4: Variogram kernel parameters.

Video	$\Delta_{nyq}$ mm	$\theta$ mm	$\nu$	$\sigma_n$ $\mu V^2$	$\zeta$ $\mu V^2$	$\lambda$ $\mu V^2$	$\Delta_{10\%}$
vid S5	1.38	3.12	1.29	43.66	4349.56	4305.90	2.15
vid S6	1.16	2.66	1.24	69.22	4647.07	4577.85	1.76
vid S7	1.25	3.43	0.78	62.49	2119.94	2057.45	1.33

Table S5: Cross-validated kriging results. Percentages relative to signal variance ( $\zeta$ ).

Video	CV err $\mu V^2$	CV err %	theor. err total %	noise %	kriging err %
vid S5	280.91	6.46	5.59	1.00	4.59
vid S6	405.20	8.72	8.67	1.49	7.19
vid S7	289.29	13.65	14.40	2.95	11.45

Table S6: High-density kriging results. Percentages relative to process variance ( $\lambda$ ). (These are estimates only, and not measurable.)

Video	on-site err $\mu V^2$	on-site err %	off-site err $\mu V^2$	off-site err %
vid S5	31.23	0.73	49.62	1.15
vid S6	50.68	1.11	85.74	1.87
vid S7	45.37	2.21	94.70	4.60

### 4.3 Human motor cortex bandpasses (supplemental videos S8-S12)

Kernel estimates and kriging statistics in tables 7-9.

Table S7: Variogram kernel parameters.

Video	$\Delta_{nyq}$ mm	$\theta$ mm	$\nu$	$\sigma_n$ $\mu V^2$	$\zeta$ $\mu V^2$	$\lambda$ $\mu V^2$	$\Delta_{10\%}$
vid S8 (4-7 Hz)	0.95	2.10	1.37	0.97	102.47	101.50	1.51
vid S10 (15-30 Hz)	1.08	2.35	1.40	0.96	83.36	82.39	1.72
vid S11 (30-60 Hz)	0.71	1.69	1.12	0.75	15.53	14.78	0.93
vid S12 (75-300 Hz)	0.58	1.14	1.89	2.27	23.17	20.90	0.79

Table S8: Cross-validated kriging results. Percentages relative to signal variance ( $\zeta$ ).

Video	CV err $\mu V^2$	CV err %	theor. err total %	noise %	kriging err %
vid S8 (4-7 Hz)	16.02	15.63	10.68	0.95	9.73
vid S10 (15-30 Hz)	9.46	11.34	8.49	1.16	7.33
vid S11 (30-60 Hz)	3.72	23.98	25.92	4.81	21.12
vid S12 (75-300 Hz)	10.08	43.51	39.51	9.80	29.72

Table S9: High-density kriging results. Percentages relative to process variance ( $\lambda$ ). (These are estimates only, and not measurable.)

Video	on-site err $\mu V^2$	on-site err %	off-site err $\mu V^2$	off-site err %
vid S8 (4-7 Hz)	0.82	0.81	1.95	1.92
vid S10 (15-30 Hz)	0.74	0.90	1.30	1.58
vid S11 (30-60 Hz)	0.55	3.71	1.00	6.78
vid S12 (75-300 Hz)	1.45	6.93	1.84	8.82

## References

- [1] Carl Edward Rasmussen. *Gaussian processes for machine learning*. MIT Press, 2006.
- [2] A Destexhe, D Contreras, and M Steriade. Spatiotemporal analysis of local field potentials and unit discharges in cat cerebral cortex during natural wake and sleep states. *The Journal of neuroscience : the official journal of the Society for Neuroscience*, 19(11):4595–608, jun 1999.
- [3] David A Markowitz, Yan T Wong, Charles M Gray, and Bijan Pesaran. Optimizing the decoding of movement goals from local field potentials in macaque cortex. *The Journal of neuroscience : the official journal of the Society for Neuroscience*, 31(50):18412–22, dec 2011.
- [4] Michele Insanally, Michael Trumpis, Charles Wang, Chia-Han Chiang, Virginia Woods, Kay Palopoli-Trojani, Silvia Bossi, Robert C Froemke, and Jonathan Viventi. A low-cost multiplexed  $\mu ECoG$  system for high-density recordings in freely moving rodents. *J. Neural Eng.*, 13(2):026030, mar 2016.
- [5] Spencer Kellis, Larry Sorensen, Felix Darvas, Conor Sayres, Kevin O’Neill, Richard B Brown, Paul House, Jeff Ojemann, and Bradley Greger. Multi-scale analysis of neural activity in humans: implications for micro-scale electrocorticography. *Clinical Neurophysiology*, 127(1):591–601, 2016.

- [6] Leah Muller, Liberty S Hamilton, Erik Edwards, Kristofer E Bouchard, and Edward F Chang. Spatial resolution dependence on spectral frequency in human speech cortex electrocorticography. *Journal of neural engineering*, 13(5):056013, 2016.
- [7] Walter J Freeman and John M Barrie. Analysis of spatial patterns of phase in neocortical gamma eegs in rabbit. *Journal of neurophysiology*, 84(3):1266–1278, 2000.
- [8] Walter J Freeman, Linda J Rogers, Mark D Holmes, and Daniel L Silbergeld. Spatial spectral analysis of human electrocorticograms including the alpha and gamma bands. *Journal of Neuroscience Methods*, 95(2):111–121, feb 2000.
- [9] Marc W Slutzky, Luke R Jordan, Todd Krieg, Ming Chen, David J Mogul, and Lee E Miller. Optimal spacing of surface electrode arrays for brain–machine interface applications. *Journal of Neural Engineering*, 7(2):026004, mar 2010.
- [10] Dale L Zimmerman and Noel Cressie. Mean squared prediction error in the spatial linear model with estimated covariance parameters. *Annals of the institute of statistical mathematics*, 44(1):27–43, 1992.
- [11] Noel Cressie and Dale L Zimmerman. On the stability of the geostatistical method. *Mathematical Geology*, 24(1):45–59, 1992.
- [12] Virginia Woods, Michael Trumpis, Brinnae Bent, Kay Palopoli-Trojani, Chia-Han Chiang, Charles Wang, Chunxiu Yu, Michele N Insanally, Robert C Froemke, and Jonathan Viventi. Long-term recording reliability of liquid crystal polymer  $\mu$ ECoG arrays. *Journal of Neural Engineering*, 15(6):066024, oct 2018.
- [13] M A Gieselmann and A Thiele. Comparison of spatial integration and surround suppression characteristics in spiking activity and the local field potential in macaque V1. *The European journal of neuroscience*, 28(3):447–59, aug 2008.
- [14] Jeremy R Manning, Joshua Jacobs, Itzhak Fried, and Michael J Kahana. Broadband shifts in local field potential power spectra are correlated with single-neuron spiking in humans. *The Journal of neuroscience : the official journal of the Society for Neuroscience*, 29(43):13613–20, oct 2009.
- [15] Philipp Berens, Georgios a Keliris, Alexander S Ecker, Nikos K Logothetis, and Andreas S Tolias. Comparing the feature selectivity of the gamma-band of the local field potential and the underlying spiking activity in primate visual cortex. *Frontiers in systems neuroscience*, 2(June):2, jan 2008.
- [16] Supratim Ray, Nathan E Crone, Ernst Niebur, Piotr J Franaszczuk, and Steven S Hsiao. Neural correlates of high-gamma oscillations (60-200 Hz) in macaque local field potentials and their potential implications in electrocorticography. *The Journal of neuroscience : the official journal of the Society for Neuroscience*, 28(45):11526–36, nov 2008.
- [17] Supratim Ray and John H. R. Maunsell. Different Origins of Gamma Rhythm and High-Gamma Activity in Macaque Visual Cortex. *PLoS Biology*, 9(4):e1000610, apr 2011.
- [18] Kai J Miller, Eric C Leuthardt, Gerwin Schalk, Rajesh P N Rao, Nicholas R Anderson, Daniel W Moran, John W Miller, and Jeffrey G Ojemann. Spectral changes in cortical surface potentials during motor movement. *J. Neurosci.*, 27(9):2424–32, feb 2007.
- [19] Spencer Kellis, Kai Miller, Kyle Thomson, Richard Brown, Paul House, and Bradley Greger. Decoding spoken words using local field potentials recorded from the cortical surface. *J. Neural Eng.*, 7(5):056007, oct 2010.
- [20] Jean-Philippe Lachaux, Nikolai Axmacher, Florian Mormann, Eric Halgren, and Nathan E Crone. High-frequency neural activity and human cognition: past, present and possible future of intracranial eeg research. *Progress in neurobiology*, 98(3):279–301, 2012.